Time-resolved infrared imaging and spectroscopy for engine diagnostics

Prof. Volker Sick, Lucca Henrion, Ahmet Mazacioglu, Michael C. Gross – University of Michigan

Abstract

Molecular emissions in the infrared spectral region can provide access to a range of quantities that are of interest in internal-combustion engine research and development. Molecules; such as water, carbon dioxide, carbon monoxide, and hydrocarbons; provide the strongest signals in the range from 1.0 to 5.5 µm. We describe several imaging experiments that employed high-frame-rate infrared cameras to capture spectrally resolved and spectrally integrated signals from both optical and production engines. Spectrally resolved infrared emissions that were recorded at kHz rates (i.e., crank-angle steps) in an optically accessible, propane-fueled, single-cylinder engine are used to guide the development and validation of a radiative-emission model that is integrated into large-eddy simulations (not discussed in this paper). The emissions were dispersed with a spectrometer, and the spectra were recorded with an InSb camera. Clear spectral signatures from water and carbon dioxide were recorded, and the spectra reveal the evolution of combustion through each of 100 consecutive cycles for each engine run. Furthermore, at any wavelength of these spectra, cycle-to-cycle variation can be extracted readily. Cycle-to-cycle variation was of particular interest in a study of a production heavy-duty engine fueled by natural gas.The addition of two borescopes outfitted with high-frame-rate InGaAs cameras enabled spectrally integrated measurements from 1.0-1.7 µm. The images allow cycle-resolved observations of ignition and flame growth. The intent of this work was to identify and quantify the impact of a range of ignition systems on lean and/or dilute operation limits from a combustion development and stability point of view.

1 Introduction

The experimental study of combustion involves measuring flow, mixture composition, and temperature, among other parameters. For decades, optical diagnostic techniques (e.g., laser-induced fluorescence, laser-induced incandescence, particle-image-velocimetry, shadowgraphy, schlieren imaging) have been used to measure these quantities [1-5]. The vast majority of these measurements have been performed in or near the visible band (~0.4-0.7 µm), due to the advanced development level of optical technology in this band. Silicon is a mature material, thanks to its use in computer processors, and it offers sensitivity to wavelengths of ~0.4-1.0 µm. Lens technology is also very mature in the visible band, since consumer cameras work in the visible. By contrast, infrared (IR) imaging technology is less mature. However, imaging in the IR offers crucial benefits for combustion research. First, the blackbody radiation produced by soot [6] at combustion-relevant temperatures is much stronger in the IR than the visible. More importantly, combustion-relevant species exhibit emission lines in the wavelengths from 1.0 to 5.5 µm [7-10]. Because of the strength of these emissions, it is often possible to collect sufficient signal without using an intensifier, thus eliminating an expensive, delicate component that reduces spatial resolution. Of interest for this work, the emission lines of water and carbon dioxide can act as proxies for the flame front and burned-gas region. While water is present in the intake charge due to atmospheric humidity, it is found at higher temperature and concentration (both of which yield stronger emission) in the volume where combustion has occurred. The significant increase in water concentration (due to a peak water production rate of ~15x10-3 mol/[cm3-s] for a laminar, stoichiometric, methane/air premixed flame) and in temperature (~4-fold for a laminar, stoichiometric, methane/air premixed flame) across the thickness of the flame front, a distance of approximately 0.5 mm [11], allow water to serve as a proxy for the location of the flame front and burned-gas region [12-15]. Finally, infrared imaging can provide spatially resolved temperature measurements, though thermography is not discussed here.

Not all IR bands are equally useful. The near infrared band (NIR, 0.7-1.4 µm) offers a performance/price ratio only slightly worse than the visible band but only offers access to emission lines of water. The short-wavelength infrared (SWIR, 1.4-3 µm) is somewhat less mature but offers stronger water lines and lines of carbon dioxide, as well as imaging and thermography of objects at some higher combustion-relevant temperatures. The mid-wavelength infrared (MWIR, 3-8 µm) includes stronger water, carbon dioxide, carbon monoxide, and hydrocarbon lines as well as the opportunity for imaging/thermography of objects at lower combustion-relevant temperatures. The long-wavelength infrared (LWIR, 8-15 µm) provides imaging/thermography of objects at body temperature or room temperature (and is thus also known as the thermal band), making the LWIR less useful for combustion research.

In this paper, we present two experiments demonstrating how NIR/SWIR imaging and spectroscopy can provide critical information for both fundamental and applied combustion research.

- The first, fundamental experiment was centered on time-resolved, in-cylinder, IR emission spectroscopy and shows the promise of this technique. The main advantage of this diagnostic is the combination of the broad wavelength range measured and sufficiently fine spectral resolution to provide simultaneous, species-specific information, giving a broad understanding of the molecular radiation. This combination can provide detailed information about intra- and trans-cylinder radiative heat transfer and can also be used for validation of simulated spectra reaching the wall, similar to those reported by Fernandez et al. [16]. Further, the addition of simultaneous NIR/SWIR imaging provided information about the spatial evolution of the flame kernel.
- The second, applied experiment was centered on high-speed NIR/SWIR borescopic in-cylinder imaging, which was used to evaluate the effect of two ignition systems on flame-kernel growth and cycle-to-cycle variation (CCV).

1.1 Spectroscopy for Fundamental Heat-Transfer Research

Heat transfer in internal-combustion engines (ICEs) has been studied since the 1920s in an effort to increase engine efficiency [17]. The amount of energy lost to the cylinder walls, piston surface, and the head of the engine is significant, and production engines are designed to reduce this energy loss [18]. Efficiency can be increased by running at higher pressures.

Unfortunately, higher pressures increase the gas temperatures, which in turn yields increased heat loss and formation of NOx, a tightly regulated pollutant. Fortunately, NOx production can be mitigated through the addition of exhaust gas recirculation (EGR). EGR consists mostly of inert exhaust gases (H_2O and CO_2) that reduce the peak in-cylinder temperature and thus the formation of NOx [19]. These gases are strong emitters and absorbers in the infrared band, and radiative energy redistribution could lead to changes in local temperatures of tens of K [20].

The role of radiation is considered differently in compression-ignition (CI) and spark-ignition (SI) engines. In CI engines, the soot particles created during combustion have been studied as blackbody sources causing radiative heat loss to the walls [21-23]. However, recently, the application of accurate radiative transfer equation solvers for a CI engine showed that the combined infrared emissions of H_2O, CO_2, and CO can be higher than those of soot and that a significant fraction of this radiation is reabsorbed before reaching the walls [20]. In SI engines, because of the absence of soot, radiation has historically been considered to have little impact on heat transfer within the combustion chamber [18, 24]. However, the effects of added EGR to mitigate the negative consequences of higher operating pressure suggest that radiative heat transfer could be relevant to SI combustion. Therefore, accurate predictive models are needed to enable quantitative consideration of radiative heat transfer in advanced engine simulations [25]. Supporting the design and validation of such models requires adequate experimental data, which is sparse for the infrared band, in combination with other well-characterized data, for a comprehensive analysis of an SI engine.

The IR band and its relevance to combustion have been spectroscopically studied since the late 1800s [26] in order to better understand and control combustion. The IR band is the most relevant for assessing the redistribution of radiative energy within the combustion chamber and the transfer of energy to the walls. The strongest molecular emission lines of H_2O, CO_2, and CO are located in the NIR, SWIR, and MWIR [7-10]. A simulation of the IR emission of gases produced in SI combustion based on the High-Resolution Transmission Molecular Absorption Database (HITRAN) showed that over 80% of H_2O and CO_2 emissions occur within the 1.0-5.5 μm band [27]. Additionally, as mentioned, the blackbody emission of soot is brighter in the IR than in the visible. Although soot is a greater concern in CI engines than in SI engines, the trend toward direct injection in SI engines means that soot and its radiation is increasingly relevant to SI combustion and heat transfer.

In-situ IR spectroscopy of SI engines has been performed using methods including Fourier transform infrared spectroscopy [28, 29] and tunable diode-laser absorption spectroscopy [30, 31], yielding the concentration, temperature and the ensemble-averaged emission spectrum of the engine gases. IR absorption experiments have successfully given measurements of concentration and temperature near the spark plug but lack the ability to measure a broad emission spectrum at fine temporal resolution [32]. The method described in this paper was developed to measure a spectrally broad emission spectrum at fine temporal resolution. The technique described here offers the ability to measure the transient emissions of SI engine gases during combustion, and it has the unique ability to be translated to capture the spectrum at different spatial locations within the combustion chamber. Additionally, the technique can be adapted to provide one dimension of spatial information, i.e., line imaging, in addition to spectral information. High-speed, time-resolved diagnostic techniques performed in the visible and ultraviolet bands can be used to study temperature, equivalence ratio [33], turbulence, CCV [34, 35], and other parameters. These techniques, however, cannot directly provide information about radiative heat transfer. The work presented here is based on the premise that time-resolved IR spectroscopy of molecular radiation reaching the walls in an optically accessible engine can enable a better understanding of radiative energy redistribution and how this radiation affects other engine parameters.

1.2 Imaging for Applied Ignition Research

Leaner air/fuel mixtures are desirable for improved efficiency in SI engines, due to better thermodynamic properties of the mixture, reduced pumping work, lower heat losses from lower burned-gas temperatures, and the higher compression ratios that can be reached without knock. However, leaner mixtures require higher ignition energy and some method of accelerating the flame growth so that combustion can be completed during the time available. In order to address these requirements, Quader [36] defined two limiting parameters [37]: (i) the flame-initiation (or ignition) limit and (ii) the partial-burn limit. The first limit marks the threshold at which ignition fails, and it is affected by flame-quenching factors, such as charge dilution, mixture motion, mixture temperature, compression ratio, and spark energy, as well as the spark plug's heat range, extension, and gap. The second limit marks the boundary where the flame-propagation speed becomes too low to complete combustion after the mixture is ignited, and it is affected by charge dilution, mixture temperature, mixture turbulence, and the location and geometry of the spark. Ignition timing must be selected based on both of these limits. Advanced spark timing prevents partial burns by providing more time for the flame to propagate, but it also leads to more misfires, especially in leaner mixtures, since the temperatures and pressures early in the cycle are not high enough for flame initiation, and the turbulence level quenches the flame kernel. On the other hand, retarding the spark timing reduces the misfire risk, but it also reduces the available time for flame propagation and hence makes the combustion more susceptible to partial burn. Operating in the stable-combustion zone located between the flame-initiation and partial-burn limits becomes increasingly challenging as the mixture becomes leaner or more dilute or the combustion chamber becomes larger.

Some advanced ignition systems try to overcome the ignition limit by increasing either their output energy (e.g., dual-coil ignition [38, 39], Controlled Electronic Ignition [40]) or the effectiveness of the spark-to-gas energy transfer (microwave-assisted spark ignition [41, 42], high-frequency corona ignition [43-45], nanosecond-pulsed transient-plasma ignition [46, 47], breakdown ignition [37], laser ignition [48]). Some systems

attempt to overcome the partial-burn limit by some combination of increasing the flame-propagation rate (microwave-assisted ignition [49, 50]) or reducing the flame-travel distance within the cylinder (multi-plug ignition [51], high-frequency corona ignition [45, 52, 53], nanosecond-pulsed transient-plasma ignition [46, 47]).

High-frequency corona ignition addresses both limits and is of particular interest. This technology uses bursts of a sinusoidal electric field with a MHz carrier frequency and a MV/m amplitude to produce plasma streamers from several fine electrode tips. The period of the MHz carrier, on the order of 1 µs, does not give the ions and electrons in the plasma time to thermally equilibrate during each carrier cycle, so the electrons are heated to a much higher temperature than the ions [54]. This process repeats for each cycle in the burst, so the temperatures of the ions and electrons never equalize. Such a plasma is said to be nonthermal, nonequlibrium, or transient. The electrons are more effective than the ions at initiating the chain-branching reactions of combustion [55]. Thus, less ignition energy is wasted in heating the ions, and energy is more efficiently used to initiate combustion, which addresses the flame-initiation limit. Each electrode tip produces a streamer many millimeters long, and a wrinkled kernel forms along each streamer. As a result, the total flame volume just after ignition is much larger than for conventional ignition, the flame-travel distances are reduced, and the wrinkled flame travels at a higher speed, all of which address the partial-burn limit.

In this document, we compare the ability of conventional and high-frequency corona systems to ignite both stoichiometric, minimally diluted NG mixtures and lean, dilute NG mixtures in heavy-duty (HD) applications. The goals of this work were to determine if combustion stability at the lean operating limit could be improved and to understand the mechanism of any such improvement. The two ignition systems produce plasmas with very different spatial and temporal evolution. Therefore, direct visual observation of the ignition and flame kernel growth is of interest in this study. While optically accessible engines provide the best view of the combustion chamber, optical engines limit the peak pressure and engine speed that are attainable. Borescopes provide much more restricted access, but they can be installed in a production engine and can withstand the peak pressures reached therein. It was critical for this project to replicate real-world pressures and engine speeds, so borescopic access was chosen.

2 Setup and Procedure

2.1 Spectroscopy for Fundamental Heat-Transfer Research

The experimental setup, as illustrated in Figure 1, was used for measurements in an optically accessible engine. Spectroscopy was performed by the lenses, spectrometer, and camera shown on the right; imaging was performed by the compound lens, filter, and camera on the bottom.

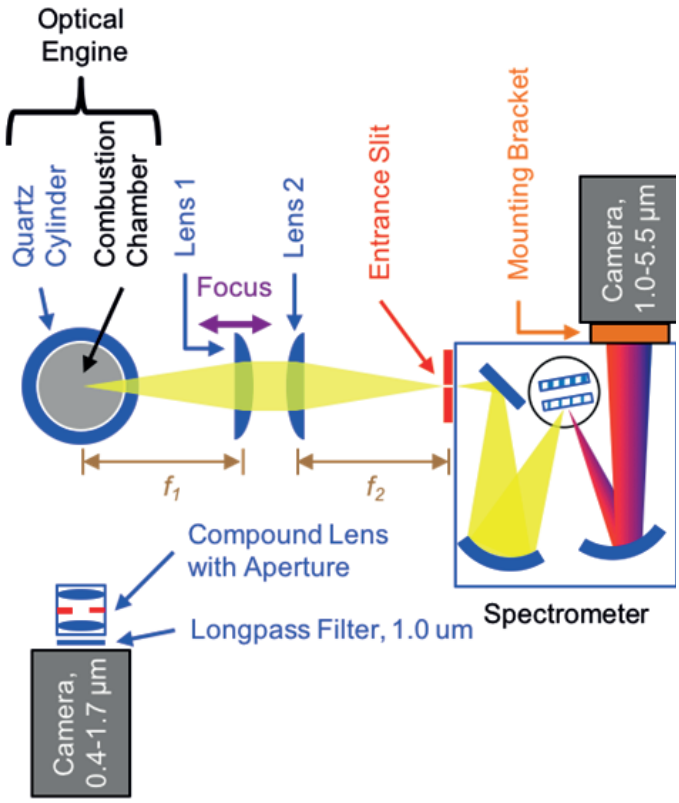

Figure 1. Infrared imaging and spectroscopy were performed simultaneously on the optically accessible engine. f1 = f2 =250 mm.

2.1.1 Optically Accessible Engine

The engine is the third-generation Transparent Combustion Chamber (TCC-III) engine, which has been described in detail elsewhere [20], [56]. This engine has a simple pancake chamber with bore x stroke of 92 mm x 86 mm, two valves, and a geometric compression ratio of 10:1. The engine was run on a homogeneous and stoichiometric propane/air mixture at 500 rev/min with pressure in the intake and exhaust plenums of 40 and 101.5 kPa, respectively. The ignition timing was -18 degrees after top dead center firing (°aTDC). The in-cylinder pressure was measured with a pressure transducer (Kistler 6125C12) every 0.5 crank-angle degrees (CAD).

A fused-silica cylinder (Rodriguez Consulting) provides optical access. The transmission of fused silica varies according to the manufacturing process, so the transmission was measured (Figure 2) using the spectroscopy setup and a blackbody source (Electro Optical Industries LES800-04) with a known emission spectrum. Although the cylinder transmits well across the visible, NIR, and SWIR bands, there is strong attenuation from around 2.75 µm and beyond 4.0 µm. As a result, the signal recorded in these bands was weak, and correcting recorded signals for these (low) measured transmission values produced unreliable results for the emission inside the cylinder. In order to avoid these regions, the work presented here only includes wavelengths shorter than 2.5 µm.

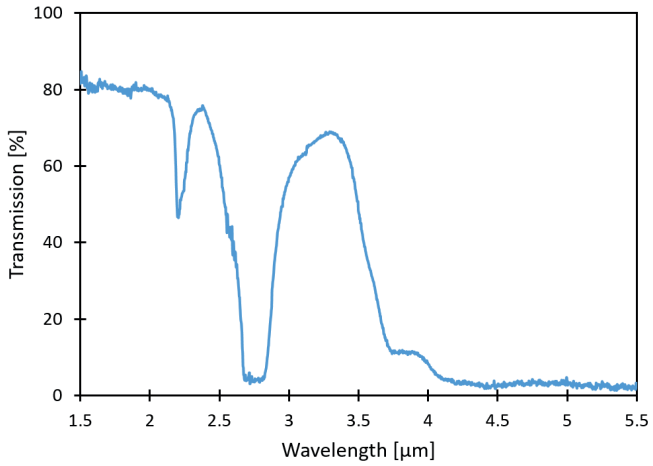

Figure 2. The measured transmission of the fused-silica cylinder. The low transmission near 2.75 μm and above 4.0 μm lead to the work described here being performed at wavelengths below 2.5 μm.

2.1.2 Cameras and Optics

Two CaF2 plano-convex lenses (focal length = 250 mm) were used to focus the light from the combustion chamber onto the spectrometer's entrance slit. The focal point was ~10 mm below the center of the cylinder head, where the spark plug is located. The spectrometer (McPherson Model 2035) had a 350-mm focal length on the input mirror. An output mirror with a 400-mm focal length was selected to place the output image on the camera sensor when the camera was mounted via a custom bracket to the spectrometer's output port. All of the spectrometer's mirrors were gold-coated to provide the best reflection across the wide range of wavelengths investigated. The spectrometer was equipped with two turret-mounted gratings (Richardson), but only the grating blazed at 4.0 μm with a density of 11.5 groove/mm was used for these experiments.

The high-speed IR camera used with the spectrometer (Xenics Onca MWIR InSb 320 with broadband option) has an InSb sensor with 320 x 256 pixels sensitive from 1.0 to 5.5 μm. The camera records at 460 Hz full frame, but for the current experiments, the camera was windowed to 320 x 8 pixels, allowing frame rates up to 3.5 kHz. A two-brightness nonuniformity correction was performed using an integrating sphere (Electro Optical Industries ISV-400S), though an aperture inside the camera partially blocks 132 pixels, some on each side of the sensor; signals from those pixels were discarded. The spectral sensitivity of the spectrometer/camera system was measured using a blackbody source (Electro Optical Industries LES800-04), and the result was used to correct the measured spectra. A wavelength calibration was performed using a xenon lamp (Newport 6033). The IR transitions of xenon [57] were used to establish a wavelength-to-pixel mapping for each recorded spectrum. For each measurement, spectra were recorded every 1.0 CAD (giving a frame rate of 3.0 kHz) from -150 to +180 °aTDC for 100 continuous cycles. For each experiment, an average background image was recorded immediately before the data images with the same imaging parameters as the data images but without firing the engine. The background image was then subtracted from each data image to correct for background emission. Finally, the eight pixels in each column of each frame were averaged to reduce noise and create a final spectrum measuring 188 x 1 pixels.

The camera used for imaging (Xenics Cheetah-640-CL with VisNIR option) has 640 x 512 monochrome pixels with 12 bits of depth, and it is sensitive to wavelengths between 0.4 and 1.7 μm (though maximum sensitivity occurs between 1.0 and 1.6 μm). In order to better match the spectral range of the spectroscopy camera, a 1000-nm long-pass filter (ThorLabs FELH1000) was inserted between the lens (Navitar SWIR-35) and camera. The camera can operate at up to 865 Hz in full-frame mode. Unlike the spectroscopy camera, this camera was not windowed, so custom electronics were used to extract every fourth trigger, producing images at 4-CAD resolution (giving a frame rate of 750 Hz) from -150 to +180 °aTDC. This camera's images were processed according to the procedure outlined in Section 2.2.3 [58, 59].

Synchronization and triggering was accomplished with a timing unit (LaVision HSC, programmed with a Windows computer running LaVision DaVis 8). One-per-cycle and 7200-per-cycle encoder signals were provided to the timing unit. Images were acquired from the cameras with manufacturer-supplied software (Xenics Xeneth).

2.2 Imaging for Applied Ignition Research

Previous studies with a different research focus used the same experimental setup and image-processing procedure [58, 59]; thus the setup will be briefly summarized here.

2.2.1 Engine and Calibration

The test engine was a Weichai WP10NG, a turbocharged in-line six-cylinder engine with a bore x stroke of 126 mm x 130 mm, two valves per cylinder, and central-point injection of natural gas (NG). This engine had a separate cast-steel head for each cylinder, each equipped with an in-cylinder pressure transducer (AVL GH13P). The intake/exhaust plumbing was modified to enable high-pressure exhaust-gas recirculation. Two ignition systems were tested: a conventional inductive-discharge ignition system delivering 65 mJ of energy to each spark event and a high-frequency corona ignition system (BorgWarner EcoFlash). For each operating point, the spark timing was adjusted to position the crank angle at which 50% of the mass fraction of the fuel has been burned, MFB50, at approximately 9 °aTDC. (In this document, MFBx refers to the crank angle at which x% mass fraction of the fuel has been burned.) This target value was determined by earlier spark-timing sweeps at various operating points as the MFB50 that minimized brake specific fuel consumption.

2.2.2 Optical Access and Imaging Equipment

Cylinder 6, the most accessible cylinder, was modified to provide optical access for two cameras, as illustrated in Figure 3; two borescope sleeves were installed in the head, and reliefs were cut into the top of the piston to provide clearance. To reduce reflections of light produced by the flame, the piston top and head were painted with flat black high-temperature coating (VHT Flameproof). The results presented here were all selected from Camera 1 (Xenics Cheetah, as described in Section 2.1). The borescopes (AVL TKSASTA.01) measure 7 mm in outside diameter and provide an angular field of view (FoV) of 70°. The borescopes were cooled with air at six-bar pressure that was filtered to remove particles that could clog the cooling channels. The borescopes were protected from combustion heat and pressure by sapphire windows. The borescopes transmit light from visible, NIR, and SWIR but their focus is optimized over 1.0-1.7 µm; a 1.0-µm long-pass filter was inserted between the borescope and camera to provide the clearest images. The FoV of the borescope did not fill the camera sensor, and thus the camera was windowed to 384 x 336 pixels to enable higher frame rates. The camera was fixed in place by a combination of commercial (AVL) and custom-fabricated brackets. One-per-cycle and 1440-per-cycle signals were input to a timing unit (LaVision PTU-X, operated with LaVision Davis 8), which triggered the cameras.

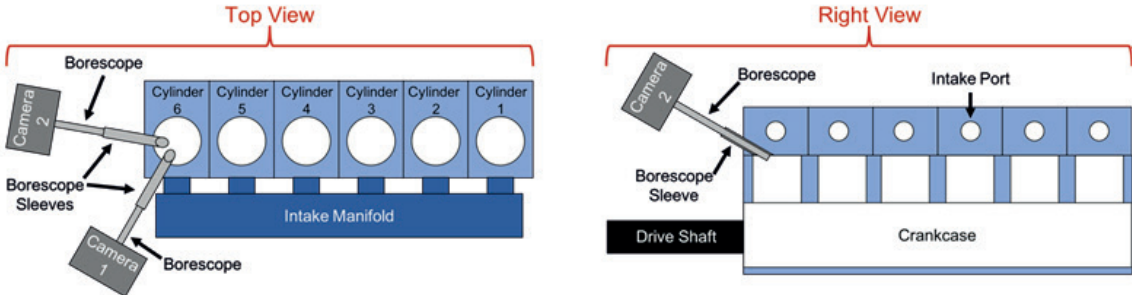

Figure 3. The experimental setup used with the production engine. Only images from Camera 1 are discussed.

2.2.3 Data and Image Acquisition

The operating points discussed here are shown in Table 1. All four points were measured at 1000 rev/min with a 6.8-bar indicated mean effective pressure (IMEP) in Cylinder 6. Two air/fuel/EGR mixtures were tested for each igniter. The EGR values of 3% were measured with the EGR valve closed and represent the minimum attainable. This nonzero value resulted from residual in-cylinder gases and possibly from exhaust-gas leakage past the EGR valve. At each operating point, the in-cylinder pressure and images were recoded over a 100-cycle period. Images were recorded at intervals of 5.5 CAD (a frame rate of 1.09 kHz). To provide more finely time-resolved information, ten measurements were made for each operating condition, each with the timing of the first image offset by a multiple of 0.5 CAD, as illustrated in Figure 4. The images from each "offset" cannot simply be interleaved to fill in the gaps in the imaging, due to CCV. However, the 100 cycles from each offset can be used to provide statistical information at 0.5-CAD intervals, as described below. During each cycle, images were recorded from just before spark timing to the point at which the FoV was nearly filled. Only data between spark timing and MFB00.5 is reported here.

2.2.4 Image Processing and Analysis

The image processing and analysis, performed with a combination of LaVision DaVis 8 and MathWorks MATLAB R2014b, has been described in detail and illustrated elsewhere [58, 59]. First, a background image recorded immediately before ignition was subtracted from each image, reducing noise. A median filter with a 3x3-pixel window was applied to smooth the image while preserving the edges. Some reflections from the piston were still visible, despite the matte black coating. To reduce these reflections, Otsu's thresholding method [60] was applied, creating a binarized image. The filtered image was multiplied by the binarized image to create the final image.

Ignition System	Air/Fuel Equiv. Ratio []	EGR [%]	Spark Timing [°aTDC]	mean($MFB_{00.5}$) [°aTDC]	Ignition Delay [CAD]	Comb. Duration [CAD]	CoV(IMEP) [%]
Conventional	1.0	3	-18.75	-2.51	16.5	15.2	0.3
	1.6	10	-52.50	-6.11	47.1	34.1	3.0
Corona	1.0	3	-13.35	-2.01	11.7	15.0	0.4
	1.6	10	-35.10	-7.85	27.7	30.7	1.9

Table 1. Engine operating conditions and parameters measured. Engine speed was 1000 rev/min; IMEP was 6.8 bar. Cases with 3% EGR occurred with the EGR valve closed.

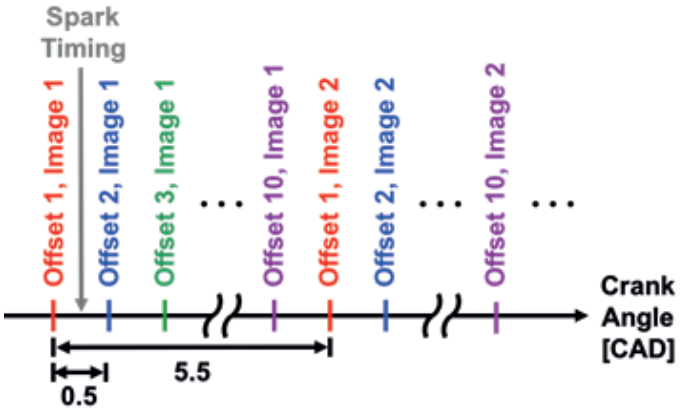

Figure 4. An illustration of the crank angles at which images were recorded. Images from each subset were recorded in a single 100-cycle measurement. Successive subsets were recorded in successive measurements moments later.

The collection of all the images recorded at a given crank angle during each 100-cycle measurement is called a "subset" in this document. Each subset of thresholded images was averaged, creating a mean image for each crank angle. The standard deviation of all the binarized images in select subsets was computed; the binarized image was chosen as the source of this calculation in order to avoid complications due to saturation. Using the binarized images also yielded standard-deviation images that were automatically normalized to a scale of 0-0.5. A number of quantitative metrics were computed from the images, as described below.

The total integrated image signal, S, was defined as the sum of the counts in all pixels of a thresholded image. S, being essentially the total brightness of the flame in the 1.0- to 1.7- μm band, should be strongly dependent on the temperature and concentration of water in the flame. It is therefore expected that S should be correlated with the timing of major combustion landmarks.

The area moment of inertia (also called the second moment of area), I, was computed by the formula below for an MxN-pixel image, where cm,n is the pixel intensity at mth row and nth column and (xc, yc) is the centroid location. I is a measure of how much "mass" (number of pixels weighted by signal strength) a flame image has and how far that mass is from the centroid.

$$I = \sum_{n=1}^{N} \sum_{m=1}^{M} c_{m,n} \times [(m - y_c)^2 + (n - x_c)^2]$$

Because very different shapes can have the same area and the same moment of inertia, the radius of gyration, rgyr, was computed by the below formula from I and the total projected area of the flame, A, in order to quantify the differences in flame shape. The radius of gyration is the radius of a point mass with the same I as the flame in the image; it is equal to the root-mean-square distance of each pixel (weighted by its brightness) from the centroid. For objects in general, rgyr is a measure of how compact or extended the object is. A circle has a small radius of gyration, while a rectangle of the same area with an aspect ratio of, e.g., 10:1 has a larger rgyr. A flame whose image has a larger radius of gyration would be expected to have a higher ratio of area to volume, in other words to be more stretched or wrinkled, and to burn more quickly. Different radii of gyration are illustrated in sample binarized flame images in Figure 5.

$$r_{gyr} = \sqrt{I/A}$$

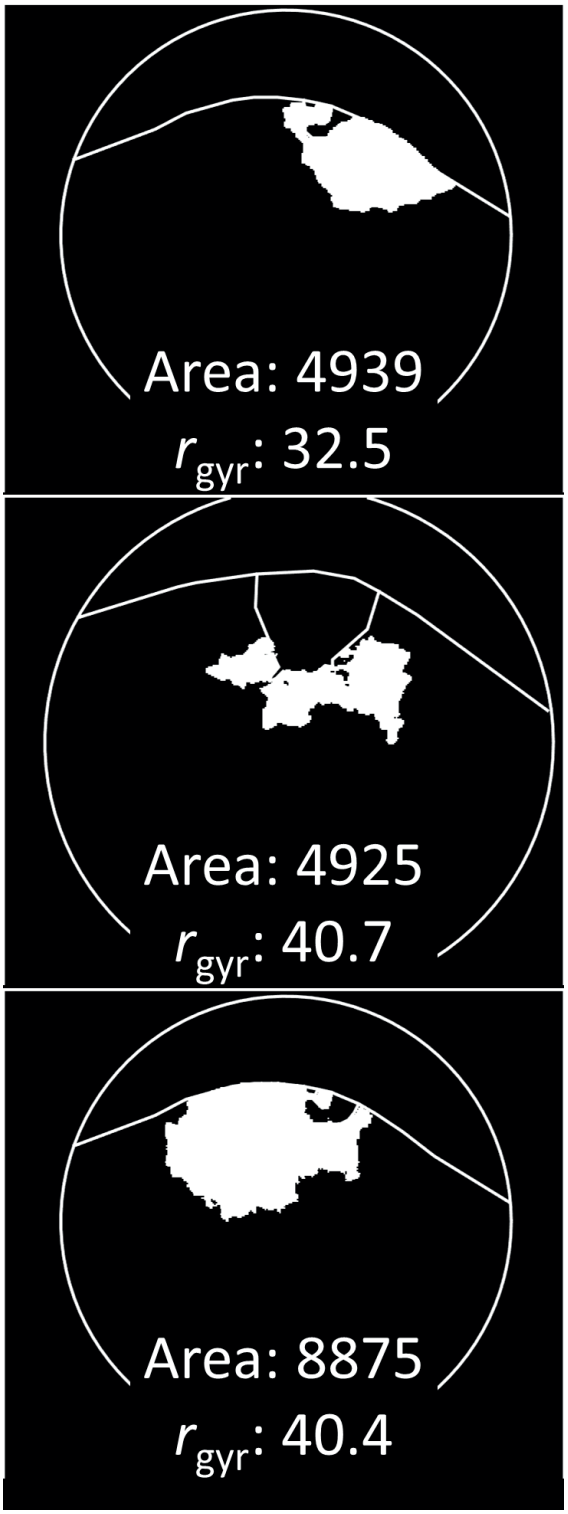

Figure 5. Binarized flame images illustrating different radii of gyration. For flames with the same area (top and middle), flames that are more spatially dispersed (middle) have higher r_{gyr} values. When both flames are similarly shaped (top and bottom), larger flames (bottom) have higher values of r_{gyr}. The units of area and r_{gyr} are pixels.

Each borescope contains a fish-eye lens at its tip, which provides a wide FoV but also distorts the images. As a result, calibrating the spatial dimensions, so that distances (e.g., r_{gyr}) can be reported in mm rather than in pixels, is not as simple as applying a linear pixel-to-mm scaling. Instead, three-dimensional dewarping must be performed. That processing has not yet been done, and all distances were calculated in pixels. It is expected that proper dewarping, once performed, will only strengthen the relationships between the image-derived and pressure-derived metrics, so the conclusions drawn here remain valid even without calibration.

It was not reasonable to compare the image-based metrics for different operating conditions at the same crank angle, since the flame development at a given crank angle would vary between conditions. Likewise, a fixed crank-angle delay relative to the spark timing was not suitable. For this document, the mean $MFB_{00.5}$ in Cylinder 6 for a given operating condition, labeled mean($MFB_{00.5}$) here, was chosen as the time at which the image-based measurements would be computed for correlation with metrics derived from the Cylinder 6 pressure transducer. This timing provided a more consistent level of flame development and ensured sufficient delay between the image- and pressure-based measurements for the results to be of interest. The symbol R(x, y) is used in this document to represent the Pearson correlation coefficient between two metrics, x and y.

In order to compare images at multiple crank angles for different operating conditions, it was necessary to determine "normalized crank angles" at which flame development was comparable across conditions. Six crank angles evenly spaced between spark timing and mean($MFB_{00.5}$) were computed for each condition, and these crank angles were labeled $\Theta_{x/5}$ where x indicated the fraction of angle between spark and mean($MFB_{00.5}$), as shown in Figure 5.

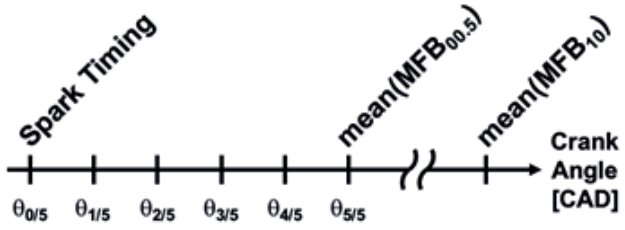

Figure 6 The normalized crank angles, $\Theta_{x/5}$, at which images from different conditions were compared.

subsets or "slices." For example, a subset of constant crank angle gives the emission spectrum at the crank angle. A subset of constant wavelength gives the time-dependent emission at that wavelength. The molecular species and vibrations can be identified from the emission spectrum and are visible in the figure. The spectroscopic range discussed in this paper, 1.3-2.5 µm, contains four water vibrations and two carbon-dioxide vibrations [13], as labeled in Figure 7. The low-amplitude feature at 1.3-1.7 µm is due to the $\upsilon_1 + \upsilon_3$ and $2\upsilon_2 + \upsilon_3$ vibrations of H_2O. The central feature at 1.7-2.2 µm is due to the $\upsilon_2 + \upsilon_3$ H_2O vibration as well as the $4\upsilon_2 + \upsilon_3$ and $\upsilon_1 + 2\upsilon_2 + \upsilon_3$ CO_2 vibrations. Finally, the feature past 2.4 µm is the beginning of the very strong υ_3 H_2O vibration.

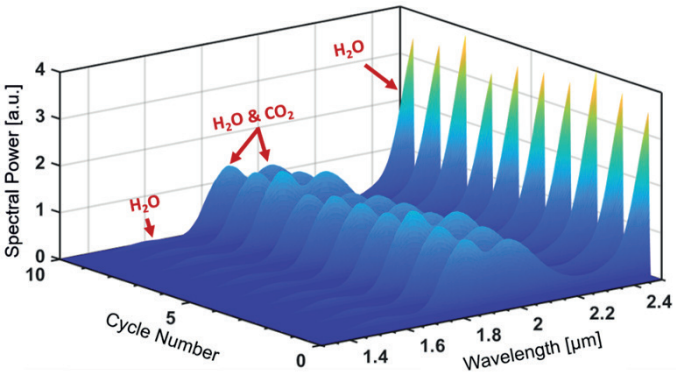

Figure 7. A three-dimensional IR emission dataset produced by the spectroscopy setup.

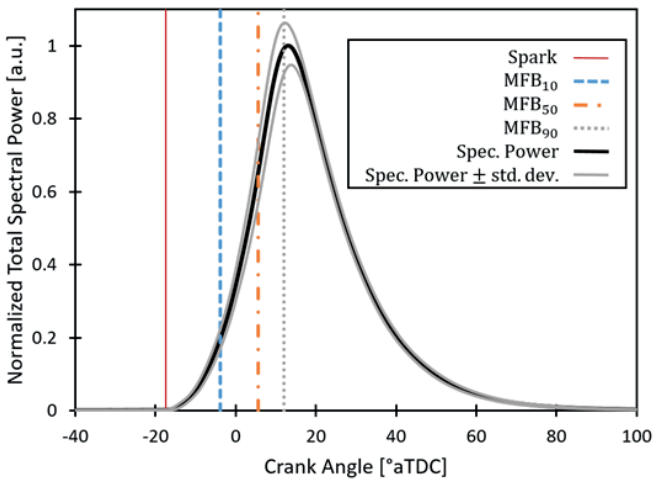

Figure 8. The normalized total optical power of the average cycle, measured with spectrometry setup. Four combustion landmarks are also shown.

3 Results and Discussion

3.1 Spectroscopy for Fundamental Heat-Transfer Research

Figure 7 shows an example three-dimensional dataset produced by the spectrometer/camera setup. For clarity, this plot shows only 10 of the 100 cycles recorded; each cycle includes spectra from -150 to +180 °aTDC. This dataset can be presented in several informative ways by displaying two-dimensional

Figure 8 was produced by computing the average and standard deviation (over all 100 cycles) of the spectrally integrated (over the entire wavelength range) emission at each crank angle. Four combustion landmarks are indicated by vertical lines. This plot illustrates how the flame emission evolves during a combustion cycle. Note that the peak emission occurs near MFB90 and that the standard deviation of the integrated emission, which is one measure of cycle-to-cycle variability, is greater before peak emission than after. This connection between the burn fraction and the molecular emission demonstrates the importance of the radiative heat released during

combustion; the rising edge of the emission curve maps to the MFB values, and the overall curve shows the timescale over which significant radiative heat transfer occurs. The relationships between these landmarks and emission peaks are further investigated in Figure 9, where a strong correlation between MFB_x and the measured spectral power is shown.

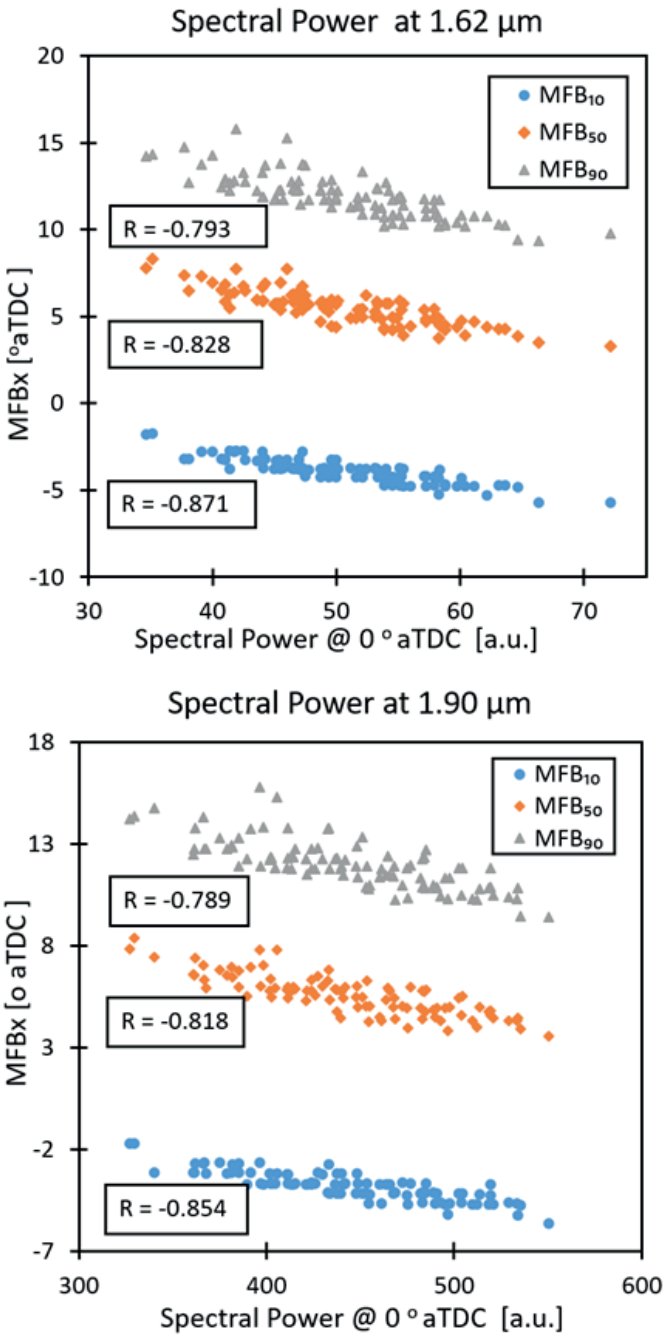

Figure 9. MFB_{10}, MFB_{50}, and MFB_{90} of each cycle correlate well with spectral power at 0 °aTDC measured at both 1.62 µm and 1.90 µm. The correlations with early MFBx values are stronger than those with later ones.

The two plots in Figure 9 show the correlation between several MFB_x values (MFB_{10}, MFB_{50}, and MFB_{90}) and the spectral power at 0 °aTDC (top dead center, TDC). The correlation is consistently high for 1.90 µm and 1.62 µm, and correlates well with the three combustion milestones; the strongest correlation for both wavelengths occurs for MFB_{10}, which has a mean location of –3.82 CAD. The higher the spectral power is at TDC the faster the combustion event occurs, hence the negative correlations with all MFB_x. The peak spectral power also correlates well with the peak in-cylinder pressure with a Pearson correlation coefficient R of 0.874 and 0.854 at 1.62 and 1.90 µm, respectively. Therefore, this diagnostic shows sensitivity to both the combustion speed and in-cylinder pressure.

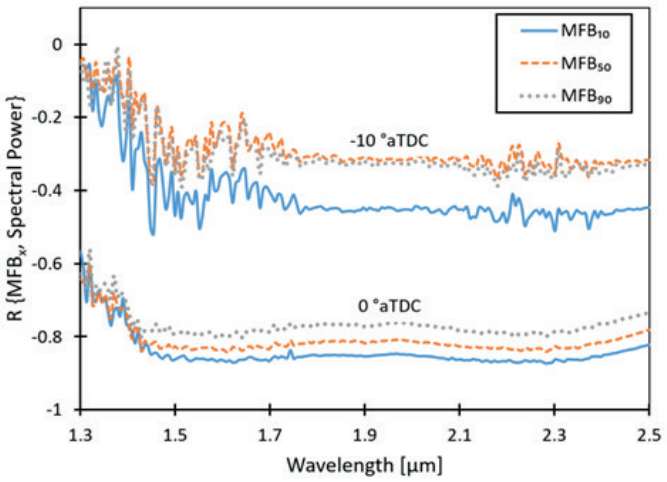

Figure 10. The correlation coefficient of MFB_x (for x = 10, 50, and 90) and spectral power at a given crank angle plotted against the wavelength at which the spectral power was measured. The bottom three curves, corresponding to spectral-power measurements made at TDC, show stronger correlations than the top three curves, corresponding to spectral-power measurements made at -10 °aTDC.

The data plotted in Figure 10 were examined to identify the wavelength at which IR signals are best correlated to combustion parameters. The top three curves show the correlations for spectral power measured at -10 °aTDC; the bottom three are for measurements at 0 °aTDC. The correlations at -10 °aTDC are lower because the flames are not yet fully developed; the early IR emission alone is not a good predictor of MFBx. However, the highest correlation for the measurements at -10 °aTDC is with early MFBx values, showing that the early flame development is well captured by this measurement. The early flame development dictates how quickly the flame will burn and the peak pressure it will produce. At 0 °aTDC, the flame is well developed, and therefore the combustion speed is already well defined, making the correlations even stronger. Even though the correlations drop for signals at wavelengths below 1.4 µm, recording signals with the Cheetah camera at wavelengths above 1.0 µm provides a good compromise between highest correlation and image quality.

Figure 11 shows that there is a strong negative correlation between spectral power measured at 1.62 µm and at 1.90 µm and IMEP. This trend shows that there is valuable information about the engine operation and its variability in the emission spectrum. For example, if the signal at TDC is high, IMEP will be lower for that cycle; this result is due to the fast combustion—compare to Figure 9 for the relationship between IR emission and MFB_x—and earlier peak pressure. The TCC-III engine is optimized to have a slower combustion, so the correlation demonstrates that if there is higher signal at TDC the peak pressure will be reached too soon and the IMEP will be negatively affected. The correlation between IMEP and IR signals at 1.62

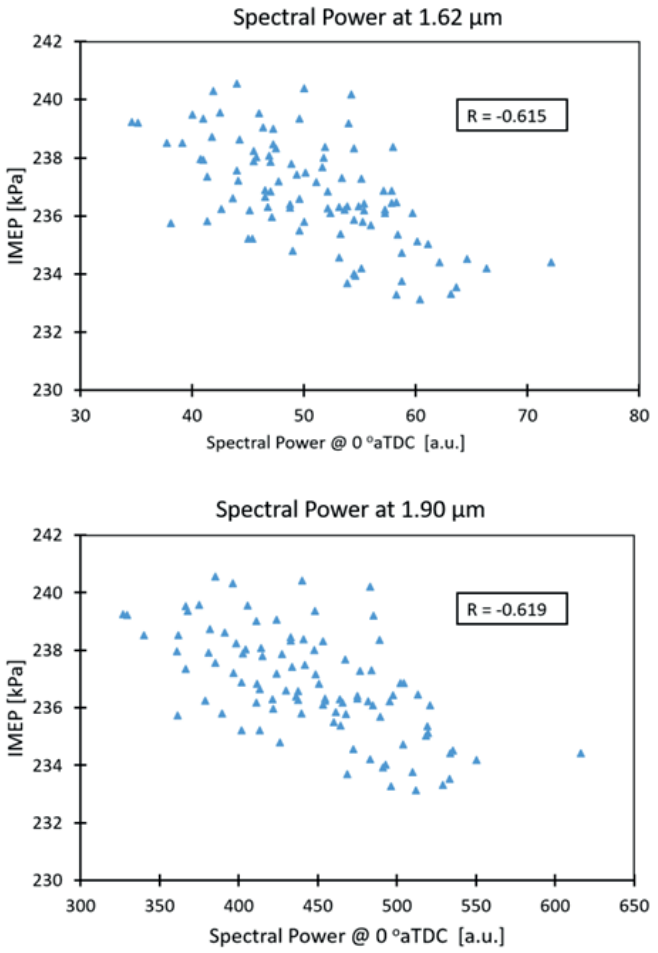

Figure 11. The IMEP of each cycle correlates well with the power measured at 1.62 µm and at 1.90 µm.

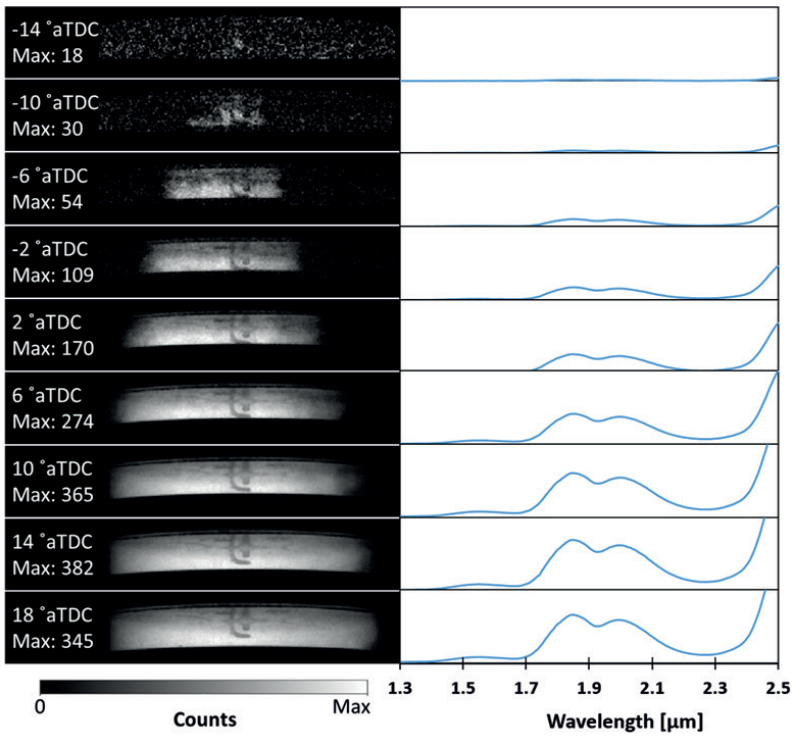

Figure 12. Images and spectra recorded simultaneously at nine crank angles within a single engine cycle.

µm and at 1.90 µm are about the same. In the following, the flame development is explored further through a combination of spectroscopy and imaging. In these experiments, the 1.3-1.7 µm region falls within the sensitivity range of both cameras. Combining spectroscopy and imaging allows spectral and spatial features of the flame to be linked.

Figure 12 shows sample images and spectra recorded simultaneously by the Cheetah and Onca cameras, respectively, at nine crank angles during a single combustion cycle. As the figure illustrates, the early flame development is captured both spatially and spectrally. The maximum image brightness and peak spectral power in Figure 12 occur at 14 oaTDC; at this time the flame has reached the cylinder wall. The signal from the Cheetah camera was summed over the clearance volume for each measured crank angle degree and compared with the total spectral power from the Onca spectra integrated over the 1.3-1.7 µm region at the corresponding crank angle. The results shown in Figure 12 demonstrate a very high correlation of R=0.996, verifying that the two measurements are correctly synchronized.

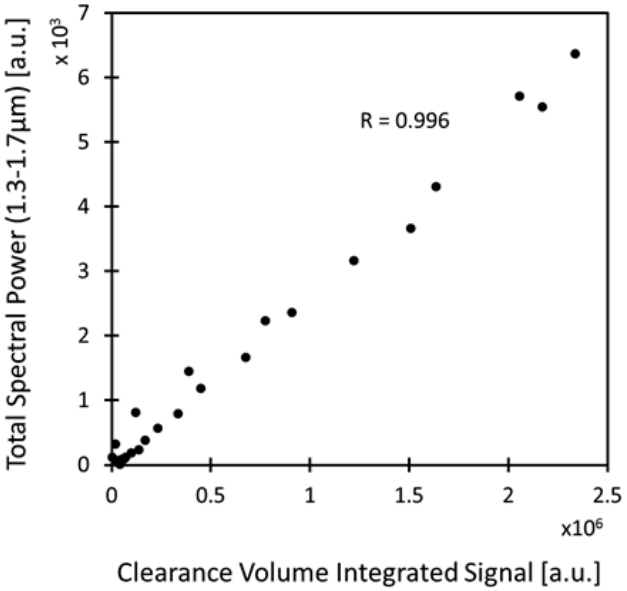

Figure 13. The spatially integrated (over the clearance volume only) signal recorded by the imaging camera correlates very strongly with the spectrally integrated signal recorded by the spectroscopy camera.

3.2 Imaging for Applied Ignition Research

Having now established the functionality of IR imaging in the NIR/SWIR band the following section describes the results of borescopic imaging in this band that was performed to study ignition in an HD engine. Figure 14 shows images recorded by Camera 1 at several crank angles for both ignition systems at a single operating condition: engine speed = 1000 rev/min, IMEP = 6.8 bar, λ = 1.0, and 3% EGR. Because the conventionally ignited flames grew more slowly than those ignited by the corona system, the timing offset between measurements was 1.0 CAD for the conventional system and 0.5 CAD for the corona system. Additionally, because the ignition timing was

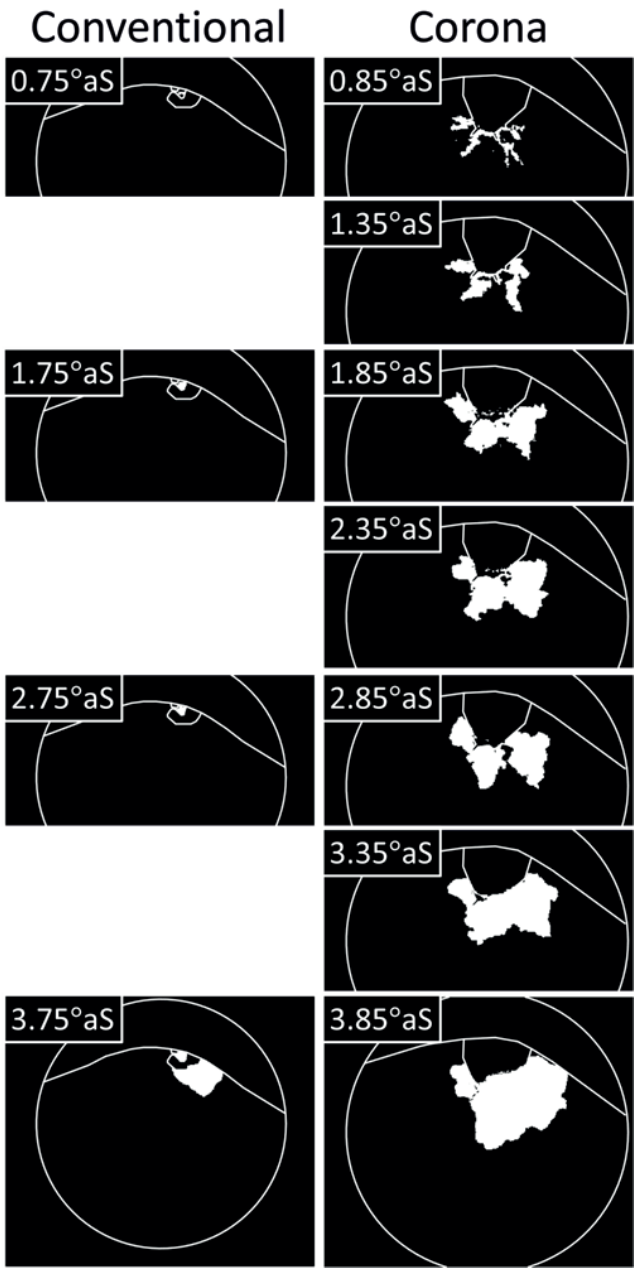

Figure 14. Binarized instantaneous image sequences of flame-kernel growth for two ignition systems. The corona system shows faster flame development. Engine speed is 1000 rev/min; IMEP = 6.8 bar; λ = 1.0, and 3% EGR. Images were taken at a lower rate for the conventional system due to the slower flame growth.

optimized for each igniter, the images for the conventional igniter were recorded beginning at 0.75 CAD after spark timing (°aS), while those for the corona system were recorded beginning at 0.85 °aS. The images illustrate the differences in how the flame kernels evolve. Each of the five streamers created by the corona igniter—the view of the rearmost one is obscured by the igniter in these images—creates a much larger, more wrinkled initial flame. These corona-ignited kernels also grow more quickly until they combine with each other. It is believed that, since the kernels are wrinkled from their inception, they skip the slow, laminar flame-growth phase and immediately enter the fast, turbulent flame-growth phase.

Figure 15 shows the standard deviation of the binarized images at five normalized crank angles (Θ1/5 through Θ5/5) for all four igniter/mixture combinations. One condition is stoichiometric with minimal (3%) EGR; the other is lean with 10% EGR. In these figures, which are false-colored according to the scale shown on the right, the band of bright (yellow) pixels represent the cycle-to-cycle variation in the flame boundary; wider bands indicate more CCV. Comparing the first column to the third and the second to the fourth reveals the bright (yellow) band is wider for the lean/dilute mixture for each igniter, indicating greater CCV for that mixture. Comparing column one to column two and column three to column four shows that the bright band is wider for the conventional system, again pointing toward greater CCV with that system. These results agree with the pressure-based measurements of CoV(IMEP), which are reported in Table 1.

Figure 16 shows how the shape of the very early flame kernels has an impact on the highly diluted flames but not the stoichiometric ones, as evidenced by the correlation between the radius of gyration measured at mean($MFB_{00.5}$) and the eventual IMEP of that cycle. This plot includes data from 100 cycles for each of the four igniter/mixture combinations. For both igniters, combustion of the stoichiometric, minimally diluted mixture is robust under variation in r_{gyr}. In other words, the shape of the very early kernel has little impact on the combustion efficacy of each cycle, leading to very small Pearson correlation coefficients. By contrast, for both igniters, combustion of the lean, dilute mixture was very sensitive to variation in r_{gyr}. Different kernel shapes resulted in different IMEPs, leading to significant correlations. Note that the sensitivity of the igniters to the early-kernel shape are very similar, as indicated by the similar correlation coefficients: 0.482 for the conventional system, 0.479 for corona.

Figure 17 presents a series of correlation plots showing the relationship between the radius of gyration measured at mean($MFB_{00.5}$) and MFB_x (for x = 5, 10, 50, 90) for 100 cycles for all four combinations of air/fuel mixture and igniter. For all four combinations and all four values of x, a negative correlation with magnitude of at least 0.497 exists. In other words, early flames with more extended or stretched shapes reach these four combustion milestones more quickly. This result agrees with expectations, since extended kernel shapes are expected to be more wrinkled and to burn more quickly. It is important to note that all four MFB values occur much later in the cycle than the time at which r_{gyr} is measured, so this measurement demonstrates predictive capability. As might be expected, the predictive capability is stronger for the earlier MFB values than the later ones.

Figure 18 shows how the correlation between MFB_{05} and the radius of gyration measured at a given crank angle changes as the crank angle of r_{gyr} measurement varies. The result is qualitatively similar for all four igniter/mixture combinations: generally negative correlations that grow stronger as the crank angle of measurement approaches mean($MFB_{00.5}$). As discussed for Figure 17, the sign of the correlation (negative) is consistent with expectations. Additionally, the most negative values of the correlation coefficient are approximately -0.8 in all cases. It is important to note, however, that there are important differences between the cases. First, the data points for the four different cases begin at different crank angles, since the spark timing was optimized for each case, as tabulated in

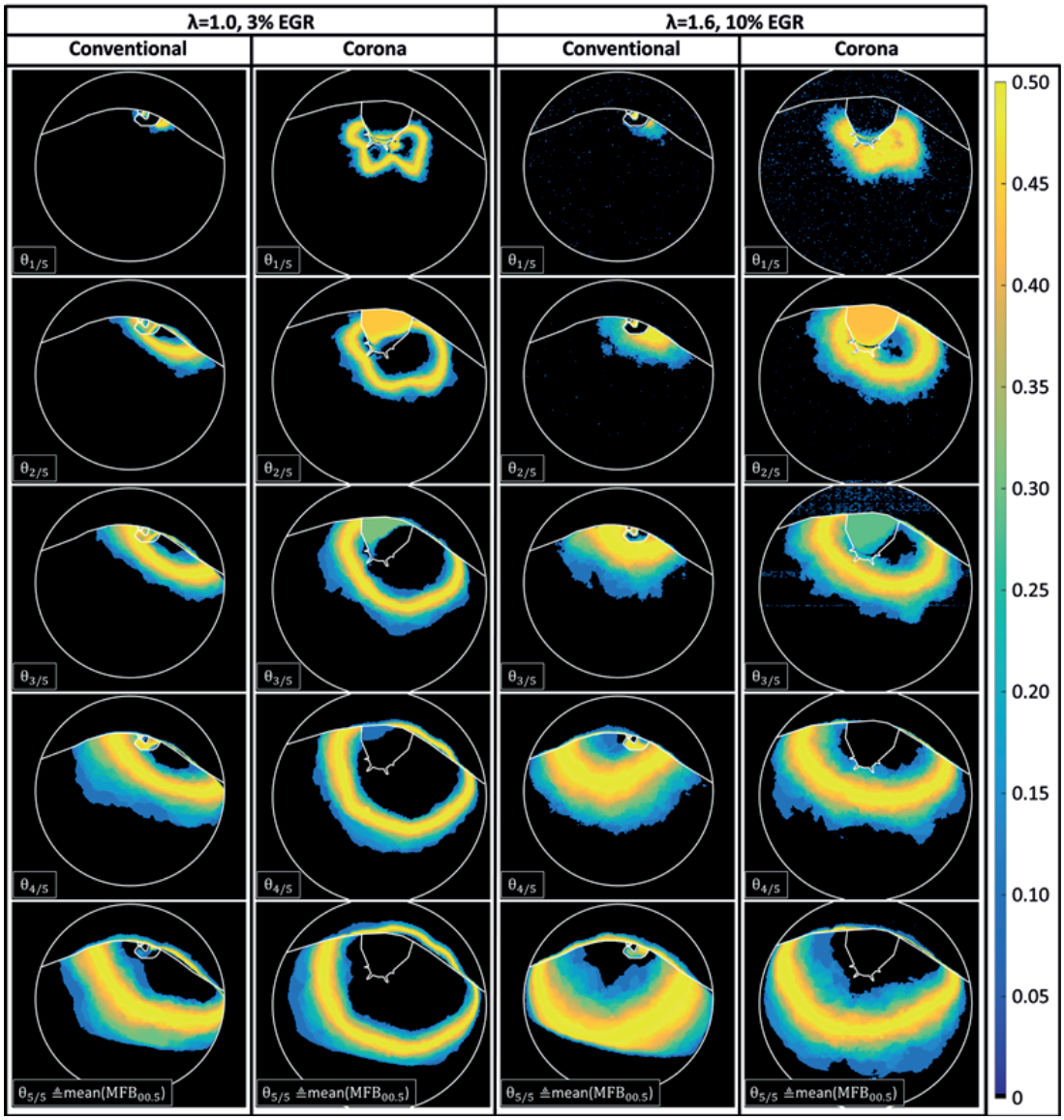

Figure 15. Standard deviation of binarized images at five normalized crank angles for two mixtures and two ignition systems. Engine speed is 1000 rev/min; IMEP = 6.8 bar. Lean, dilute mixtures yield more CCV than stoichiometric, minimally diluted mixtures, and corona-ignited flames exhibit less CCV than conventionally ignited ones. The CoV(IMEP) for each condition is, from left to right, 0.3%, 0.4%, 3.0%, and 1.9%.

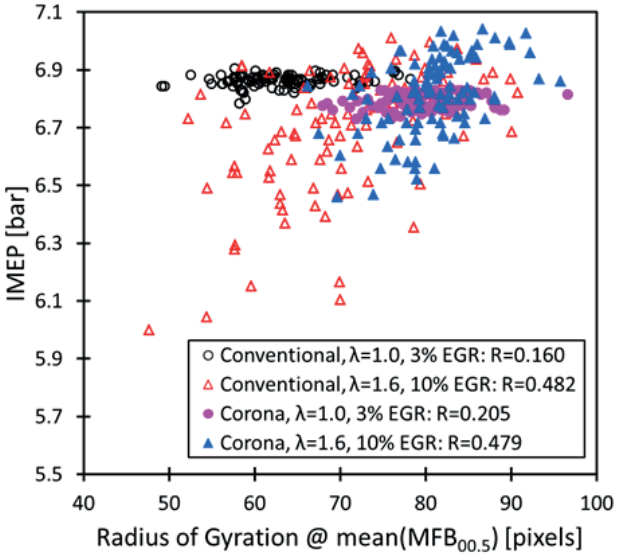

Figure 16. The IMEP of each cycle is insensitive to r_{gyr} at mean($MFB_{00.5}$) for the stoichiometric, minimally diluted mixtures, but it is sensitive to rgyr for lean, dilute mixtures.

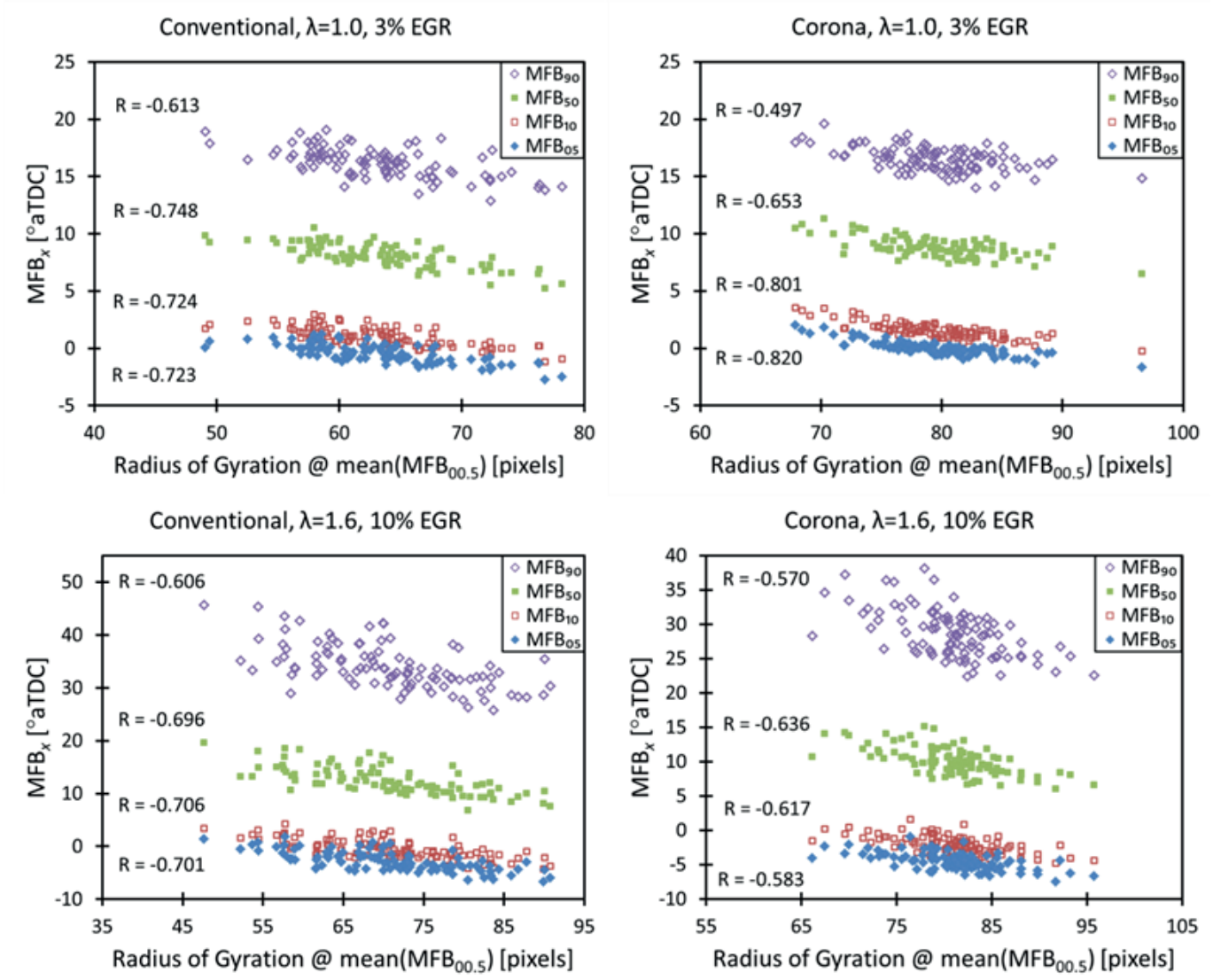

Figure 17. Correlation plots of rgyr at mean($MFB_{00.5}$) and four MFB_x values for all four igniter/mixture combinations, MFB_{05}, MFB_{10}, MFB_{x50}, and MFB_{90} are negatively correlated with the r_{gyr} measured at mean($MFB_{00.5}$). The early MFB_x values are more strongly correlated than the later ones.

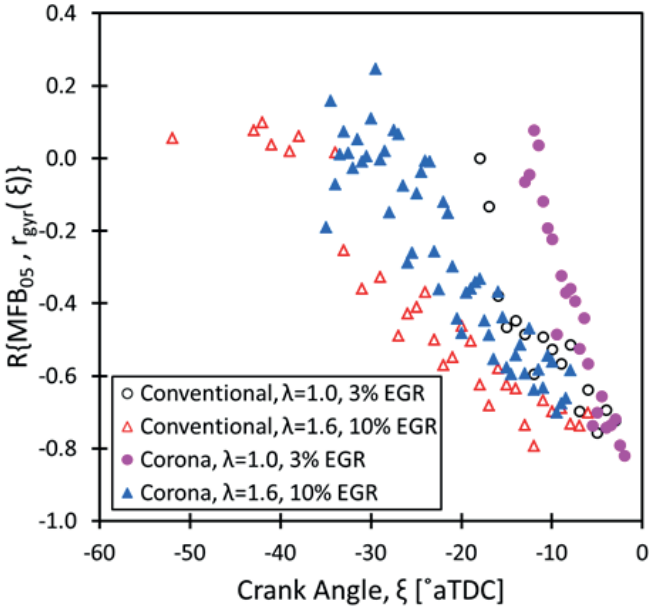

Figure 18. The negative correlation between MFB_{05} and the radius of gyration measured at a given crank angle is stronger if the r_{gyr} is measured at a later crank angle. The mean($MFB_{00.5}$) for each case is tabulated in Table 1.

Table 1. Second, for both igniters, in the stoichiometric, undiluted case, the curves are much steeper than in the lean, dilute cases. This result may be due to the flames grow much more quickly in these cases or to the combustion being less sensitive to the flame shape.

4 Summary and Conclusions

The work presented here illustrates the utility of infrared imaging and spectroscopy for internal-combustion engine research. The IR band offers two primary advantages:

- Several combustion-relevant species (e.g. H_2O, CO_2, CO, and hydrocarbons) exhibit characteristic emission lines in the NIR, SWIR, and MWIR. When spectrally and temporally resolved, this emission provides information that is unobtainable otherwise, allowing the temporal evolution of these species and their role in radiative heat transfer during the combustion cycle to be studied.
- The emissions of these species are very strong, yielding strong signals even with integration times on the order of 10 µs. The strength of the signal allows the flame size, shape, and position to be quantified with fine temporal resolution without the need for image-intensifying equipment.

Simultaneous 2D imaging and single-shot, spectrally resolved measurements were used to design an imaging strategy for applied investigations as well as for insights into the role of radiative heat transfer in spark-ignited engines. This work was conducted in the TCC-III engine and showed that spectrally resolved infrared emissions from water and carbon dioxide can be acquired at high frame rates and at spectral resolutions sufficiently fine to support simulation of in-cylinder molecular emission and absorption and the associated radiative energy redistribution.

The spectrally resolved measurements guided the selection of imaging water emissions between 1.0 and 1.7 µm in a heavy-duty, natural-gas engine. The performance of a conventional spark ignition system and a corona ignition system were compared for stoichiometric and for lean, dilute mixtures. The advantages of using a corona igniter for establishing a flame and promoting its rapid growth, even in highly dilute conditions, was directly evident from the images that were acquired via borescopic optical access. Further, a detailed analysis of the images showed that the flame development is highly sensitive to the geometric shape of the flame, illustrating the value of infrared imaging diagnostics for applied engine research and development.

Acknowledgements

The information, data, or work presented herein was funded in part by the Office of Energy Efficiency and Renewable Energy (EERE), U.S. Department of Energy, under Award Numbers DE-EE0007278 and DE-EE0007307. The University of Michigan provided Mr. Henrion with partial tuition and stipend support through the Rackham Merit Fellowship. Electro Optical Industries provided the integrating sphere and the blackbody source on loan. Mohammad Alzuabi supported experiments with the optical engine, while Justin Kern supported experiments with the production engine.

References

[1] V. Sick, „High speed imaging in fundamental and applied combustion research," Proceedings of the Combustion Institute, vol. 34, pp. 3509-3530, 2013.

[2] V. Sick, M. C. Drake, and T. D. Fansler, „High-speed imaging for direct-injection gasoline engine research and development," Experiments in Fluids, vol. 49, pp. 937-947, 2010.

[3] K. Kohse-Höinghaus and J. B. Jeffries, Eds., Applied Combustion Diagnostics. New York: Taylor and Francis, 2002, p.^pp. Pages.

[4] H. Zhao and N. Ladommatos, Engine Combustion Instrumentation and Diagnostics. Warrendale, PA: Society of Automotive Engineers, 2001.

[5] M. Raffel, C. E. Willert, S. T. Wereley, and J. Kompenhans, Particle Image Velocimetry - A Practical Guide. Goettingen: Springer-Verlag Berlin Heidelberg, 2007.

[6] S. R. Turns, An Introduction to Combustion: Concepts and Applications, 3rd ed. New York: McGraw-Hill, 2012.

[7] C. B. Ludwig, W. Malkmus, J. Reardon, J. Thomson, and R. Goulard, Handbook of infrared radiation from combustion gases. Washington, D.C.: National Aeronautics and Space Administration, 1973.

[8] J. Frank, R. Barlow, and C. Lundquist, „Radiation and nitric oxide formation in turbulent non-premixed jet flames," Proceedings of the Combustion Institute, vol. 28, pp. 447-454, 2000.

[9] S. Brookes and J. Moss, „Measurements of soot production and thermal radiation from confined turbulent jet diffusion flames of methane," Combustion and Flame, vol. 116, pp. 49-61, 1999.

[10] M. Jansons, S. Lin, and K. T. Rhee, „Infrared spectral analysis of engine preflame emission," International Journal of Engine Research, vol. 9, pp. 215-237, Jun 2008.

[11] S. R. Turns, An Introduction to Combustion, 3rd ed. New York: McGraw-Hill, 2011.

[12] A. Arakawa, K. Saito, and W. Gruver, „Automated infrared imaging temperature measurement with application to upward flame spread studies. Part I," Combustion and flame, vol. 92, pp. 222-IN2, 1993.

[13] G. Herzberg, Infrared and Raman spectra of polyatomic molecules: D. Van Nostrand Company.; New York, 1945.

[14] E. Mancaruso, L. Sequino, and B. M. Vaglieco, „IR digital imaging for analysing in-cylinder combustion process in transparent diesel engine," in Photonics Technologies, 2014 Fotonica AEIT Italian Conference on, 2014, pp. 1-4.

[15] T. McComiskey, H. Jiang, Y. Olan, K. Rhee, and J. Kent, „High-speed spectral infrared imaging of spark ignition engine combustion," SAE Technical Paper 0148-7191, 1993.

[16] S. F. Fernandez, C. Paul, A. Sircar, A. Imren, D. C. Haworth, S. Roy, and M. F. Modest, „Soot and spectral radiation modeling for high-pressure turbulent spray flames," Combustion and Flame, vol. 190, pp. 402-415, 2018.

[17] R. N. Janeway, „Combustion Control by Cylinder-Head Design," SAE Technical Paper 0148-7191, 1929.

[18] G. L. Borman and K. Nishiwaki, „Internal combustion engine heat transfer," Prog. Energy Combust. Sci., vol. 13, pp. 1-46, 1987.

[19] J. B. Heywood, „Internal combustion engine fundamentals," 1988.

[20] M. F. Modest and D. C. Haworth, Radiative heat transfer in turbulent combustion systems: theory and applications: Springer, 2016.

[21] J. Abraham and V. Magi, „Modeling radiant heat loss characteristics in a diesel engine," SAE Technical Paper 0148-7191, 1997.

[22] G. D. Ebersole, P. Myers, and O. Uyehara, „The radiant and convective components of diesel engine heat transfer," SAE Technical Paper 0148-7191, 1963.

[23] P. Flynn, M. Mizusawa, O. A. Uyehara, and P. S. Myers, „An experimental determination of the instantaneous potential radiant heat transfer within an operating Diesel engine," SAE Technical Paper 0148-7191, 1972.

[24] A. J. Torregrosa, P. C. Olmeda, and C. A. Romero, „Revising engine heat transfer," Journal of Engineering Annals of Faculty of Engineering Hunedoara, vol. 6, pp. 245-265, 2008.

[25] D. Haworth, S. Roy, J. Cai, A. Sircar, A. Imren, and M. Modest, „Modeling Radiative Heat Transfer in Engines," in International Multidimensional Engine Modelling User's Group Meeting at the SAE Congress, April, 2015.

[26] A. G. Gaydon, The Spectroscopy of Flames. New York: Wiley, 1957.

[27] L. S. Rothman, I. E. Gordon, Y. Babikov, A. Barbe, D. C. Benner, P. F. Bernath, M. Birk, L. Bizzocchi, V. Boudon, and L. R. Brown, „The HITRAN2012 molecular spectroscopic database," Journal of Quantitative Spectroscopy and Radiative Transfer, vol. 130, pp. 4-50, 2013.

[28] K. D. Rein and S. T. Sanders, „Fourier-transform absorption spectroscopy in reciprocating engines," Applied optics, vol. 49, pp. 4728-4734, 2010.

[29] K. D. Rein, S. T. Sanders, and R. J. Bartula, „Interferometric techniques for crank-angle resolved measurements of gas spectra in engines," SAE Technical Paper 0148-7191, 2009.

[30] L. A. Kranendonk, J. W. Walewski, T. Kim, and S. T. Sanders, „Wavelength-agile sensor applied for HCCI engine measurements," Proceedings of the Combustion Institute, vol. 30, pp. 1619-1627, 2005.

[31] O. Witzel, A. Klein, C. Meffert, C. Schulz, S. Kaiser, and V. Ebert, „Calibration-free, high-speed, in-cylinder laser absorption sensor for cycle-resolved, absolute H2O measurements in a production IC engine," Proceedings of the Combustion Institute, vol. 35, pp. 3653-3661, 2015.

[32] G. Rieker, H. Li, X. Liu, J. Liu, J. Jeffries, R. Hanson, M. Allen, S. Wehe, P. Mulhall, and H. Kindle, „Rapid measurements of temperature and H2O concentration in IC engines with a spark plug-mounted diode laser sensor," Proceedings of the Combustion Institute, vol. 31, pp. 3041-3049, 2007.

[33] M. Mosburger, V. Sick, and M. Drake, „Quantitative high-speed burned gas temperature measurements in internal combustion engines using sodium and potassium fluorescence," Applied Physics B, vol. 110, pp. 381-396, 2013.

[34] P. Schiffmann, „Root Causes of Cycle-to-Cycle Combustion Variations in Spark Ignited Engines," 2016.

[35] P. Schiffmann, D. L. Reuss, and V. Sick, „Empirical investigation of spark-ignited flame-initiation cycle-to-cycle variability in a homogeneous charge reciprocating engine," International Journal of Engine Research, p. 1468087417720558, 2017.

[36] A. A. Quader, „What limits lean operation in spark ignition engines-flame initiation or propagation?," SAE Technical Paper 0148-7191, 1976.

[37] J. D. Dale, M. Checkel, and P. Smy, „Application of high energy ignition systems to engines," Progress in Energy and Combustion Science, vol. 23, pp. 379-398, 1997.

[38] T. Alger, J. Gingrich, B. Mangold, and C. Roberts, „A continuous discharge ignition system for EGR limit extension in SI engines," SAE International Journal of Engines, vol. 4, pp. 677-692, 2011.

[39] G. Ruan, D. Kienzle, D. Roth, and M. Becker, „Dual coil ignition for gasoline EGR engines," MTZ worldwide, vol. 74, pp. 18-21, 2013.

[40] M. Brandt, A. Hettinger, A. Schneider, H. Senftleben, and T. Skowronek, „Extension of Operating Window for Modern Combustion Systems by High Performance Ignition," in Ignition Systems for Gasoline Engines: 3rd International Conference, November 3-4, 2016, Berlin, Germany 3, 2017, pp. 26-51.

[41] Y. Ikeda, A. Nishiyama, H. Katano, M. Kaneko, and H. Jeong, „Research and Development of Microwave Plasma Combustion Engine (Part II: Engine Performance of Plasma Combustion Engine),“ 2009.

[42] B. Wolk, A. DeFilippo, J.-Y. Chen, R. Dibble, A. Nishiyama, and Y. Ikeda, „Enhancement of flame development by microwave-assisted spark ignition in constant volume combustion chamber,“ Combustion and flame, vol. 160, pp. 1225-1234, 2013.

[43] S. Bohne, G. Rixecker, V. Brichzin, and M. Becker, „High-Frequency Ignition System Based on Corona Discharge,“ MTZ worldwide, vol. 75, pp. 30-35, 2014.

[44] D. I. Pineda, B. Wolk, J.-Y. Chen, and R. W. Dibble, „Application of Corona Discharge Ignition in a Boosted Direct-Injection Single Cylinder Gasoline Engine: Effects on Combustion Phasing, Fuel Consumption, and Emissions,“ 2016.

[45] A. Schenk, G. Rixecker, and S. Bohne, „Results from Gasoline and CNG Engine Tests with the Corona Ignition System EcoFlash,“ in Laser Ignition Conference, 2015, p. W4A. 4.

[46] C. D. Cathey, T. Tang, T. Shiraishi, T. Urushihara, A. Kuthi, and M. A. Gundersen, „Nanosecond plasma ignition for improved performance of an internal combustion engine,“ IEEE Transactions on Plasma Science, vol. 35, pp. 1664-1668, 2007.

[47] D. L. Wisman, S. D. Marcum, and B. N. Ganguly, „Chemi-ion-current-induced dissociative recombination in premixed hydrocarbon/air flames,“ Journal of Propulsion and Power, vol. 24, pp. 1079-1084, 2008.

[48] T. X. Phuoc, „Laser-induced spark ignition fundamental and applications,“ Optics and Lasers in Engineering, vol. 44, pp. 351-397, 2006.

[49] E. G. Groff and M. K. Krage, „Microwave effects on premixed flames,“ Combustion and flame, vol. 56, pp. 293-306, 1984.

[50] H. Jaggers and A. Von Engel, „The effect of electric fields on the burning velocity of various flames,“ Combustion and Flame, vol. 16, pp. 275-285, 1971.

[51] N. Nakamura, T. Baika, and Y. Shibata, „Multipoint spark ignition for lean combustion,“ SAE Technical Paper 0148-7191, 1985.

[52] [T. Briggs, T. Alger, and B. Mangold, „Advanced ignition systems evaluations for high-dilution SI engines,“ SAE International Journal of Engines, vol. 7, pp. 1802-1807, 2014.

[53] M. K. Das and S. T. Thynell, „Corona, Spark, and Electrothermal-Chemical Plasma Ignition Systems,“ Handbook of Combustion, 2010.

[54] R. J. Goldston and P. H. Rutherford, Introduction to plasma physics: CRC Press, 1995.

[55] A. Rousso, S. Yang, J. Lefkowitz, W. Sun, and Y. Ju, „Low temperature oxidation and pyrolysis of n-heptane in nanosecond-pulsed plasma discharges,“ Proceedings of the Combustion Institute, vol. 36, pp. 4105-4112, 2017.

[56] P. Schiffmann, D. L. Reuss, and V. Sick. The TCC Engine Collection. Available: https://deepblue.lib.umich.edu/data/collections/8k71nh59c

[57] C. J. Humphreys and E. Paul, „Interferometric Wavelength Determinations in the First Spectrum of 136 Xe,“ JOSA, vol. 60, pp. 1302-1310, 1970.

[58] M. C. Gross, A. Mazacioglu, J. Kern, and V. Sick, „Infrared borescopic analysis of natural-gas ignition and combustion variability,“ SAE Technical Paper 2018-01-0632, 2018.

[59] A. Mazacioglu, M. C. Gross, J. Kern, and V. Sick, „Infrared borescopic evaluation of high-energy and long-duration ignition systems for lean/dilute combustion in heavy-duty natural-gas engines,“ SAE Technical Paper 2018-01-1149, 2018.

[60] N. Otsu, „A threshold selection method from gray-level histograms,“ IEEE transactions on systems, man, and cybernetics, vol. 9, pp. 62-66, 1979.